Resin and steel-reinforced resin used as injection materials in bolted connections

Xin, Haohui; Nijgh, Martin; Veljkovic, Milan

DOI
10.1016/B978-0-12-818961-0.00023-5

Publication date
2020

Document Version
Final published version

Published in
New Materials in Civil Engineering

Citation (APA)
Xin, H., Nijgh, M., & Veljkovic, M. (2020). Resin and steel-reinforced resin used as injection materials in bolted connections. In P. Samui, D. Kim, N. R. Iyer, & S. Chaudhary (Eds.), *New Materials in Civil Engineering* (pp. 717-743). Elsevier. https://doi.org/10.1016/B978-0-12-818961-0.00023-5

Resin and steel-reinforced resin used as injection materials in bolted connections

23

Haohui Xin, Martin Nijgh and Milan Veljkovic
Faculty of Civil Engineering and Geosciences, Delft University of Technology, Delft, The Netherlands

23.1 Introduction

The joints and connections play an important role in the construction of steel structures. It is common practice to use mechanical fasteners such as bolts to join the elements of a steel structure on site. Bolted connections in steel structures are generally fabricated with hole clearances for easy assembling. The clearances can lead to some slips occurring in the joints, making the bolted connection slip-critical [1] under static or dynamic loading.

Conventional methods, including rivets, fitted bolts, or preloaded high-strength friction grip (HSFG) bolts, are generally used to improve the slip resistance. Injection bolts are regarded as a suitable alternative for a renovation of conventional connections of large-span structures [2–4]. As shown in Fig. 23.1, injection bolts are bolts in which the cavity produced by the clearance between the bolt and the wall of the hole is completely filled up with a two-component resin. Filling of the clearance is carried out through a small hole in the head of the bolt. After injection and complete curing, the connection is slip resistant [5]. Injection bolts also have the advantage that no sudden large displacements occur in the case of overloading compared with HSFG bolts [7].

The applications of injection bolts include not only repairing of old riveted structures and new construction [5,6,8]. Damaged riveted connections have been replaced with injection bolts in the Netherlands since the 1970s [8]. The choice for using resin-injected bolted connections as a replacement rather than using new rivets lies in the fact that riveting is no longer a very common connection method. As shown in Fig. 23.2, a successful application of injection bolts to repair a riveted structure was performed on the bridge “Schlossbrücke Oranienburg” [3] in Germany. In addition, injection bolts have been successfully applied for compact connections in a glass roof structure near Amsterdam Central Station [5]. The rotations introduced with normal bolted connections were too large. Injection bolts have been applied successfully in this application to limit rotations in the connections of the glass roof structure. In order to prevent connection slippage at the connection between the truss and ball bearing in Maeslant Storm Surge Barrier [6] in

New Materials in Civil Engineering. DOI: https://doi.org/10.1016/B978-0-12-818961-0.00023-5

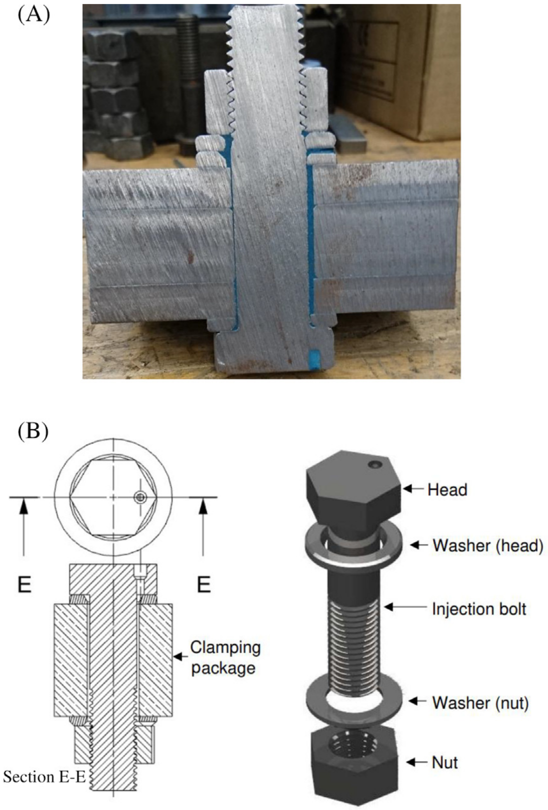

Figure 23.1 The injected bolts: (A) Photo [5]; (B) Schematic [6].

the Netherlands, resin-injected preloaded bolts have been used of metric sizes M56, M64, M72, and M80.

In the ECCS recommendations for injection bolts [7], the design bearing stress is determined based on long-duration testing. The slip for the serviceability limit state verification is suggested to be smaller than 0.3 mm [7]. Since resins are susceptible to creep deformation if the bearing stress is too high, the bearing stress needs to be kept within certain limits. Recently, the injection material, typically an epoxy resin, was modified at TU Delft by adding steel shots (spherical particles) to mitigate the effects of resin compliance in the shear connection of reusable composite (steel−concrete) structures [6], as shown in Fig. 23.3. The steel shots serve as reinforcement to the epoxy resin matrix. The increase in compressive strength and the expected improvement of creep characteristics of the reinforced injected materials, especially in a bolt hole serving as nature confinement environment, are expected to improve the performance of connections exposed to monotonic and cyclic loading.

In addition to experimental research, numerical simulations could play an important role in the qualification and certification of the short- and long-term behavior of

Figure 23.2 Corrosion of steel structure and subsequent repair with injection bolts [5].

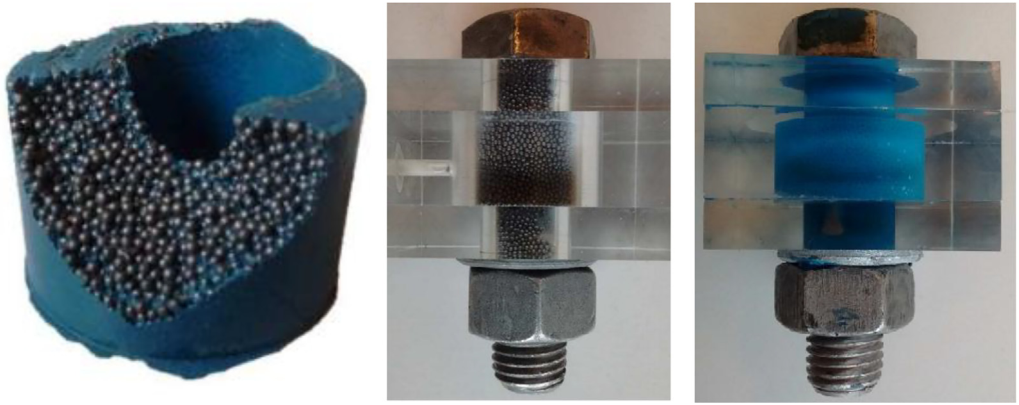

Figure 23.3 Steel-reinforced resin [6].

injection bolts. The material models of resin/steel-reinforced resin should be investigated before conducting finite element simulation on injection bolts. It is important to adopt a multiscale analysis to determine the mechanical properties of the steel-reinforced resin. The numerical homogenization method [9], which accurately considers the geometry and spatial distribution of the phases, and also precisely estimates the propagation of damage to accurately predict the failure strength [10–12], is considered to be an effective modeling tool to analyze steel-reinforced resin.

Computational homogenization methods of fine-scale models provide a pathway to use high-fidelity models (HFMs) to predict macroscopic mechanical responses of steel-reinforced resin. However, the high-fidelity numerical homogenization methods are reported to be computationally expensive [13–16]. The hierarchical strategy, where experimental results and HFM are employed to train a low-fidelity model (LFM) and to supplement the experimental database, is adopted to model the material behavior of steel-reinforced resin [13]. The performance of the steel-reinforced resin is effectively predicted by an elaborate but computationally inexpensive LFM identified by a more fundamental but computationally taxing HFM, which was calibrated to the experimental results.

Experimental compressive material tests on unconfined/confined resin and steel-reinforced resin are evaluated in this chapter. The uniaxial model which combines damage mechanics and the Ramberg–Osgood relationship is proposed to describe the uniaxial compressive behavior of resin and steel-reinforced resin. First-order numerical homogenization is employed as a HFM, where a combined nonlinear isotropic/kinematic cyclic hardening model is employed to define the steel plasticity, the linear Drucker–Prager plastic criterion was used to simulate resin damage, and the cohesive surfaces reflecting the relationship between traction and displacement at the interface. The linear Drucker–Prager plastic model is used as a LFM.

23.2 Computational homogenization

The link between microscale and macroscale behavior is established based on the Hill–Mandel computational homogenization method. The macroscale Cauchy stress σ_{ij} is obtained by averaging the microscale Cauchy stress, $\tilde{\sigma}_{ij}$, in the unit cell domain, expressed as [9]:

$$\sigma_{ij} = \frac{1}{|\Theta|}\int_{\Theta} \tilde{\sigma}_{ij} d\Theta \tag{23.1}$$

where σ_{ij} is the macroscale Cauchy stress, $\tilde{\sigma}_{ij}$ is the microscale Cauchy stress, and Θ is the domain of the unit cell. The unit cell problem is solved for the leading order translation-free microscale displacement. The microscale displacement $u_i^f(x, y)$ is expressed in the form [9]:

$$u_i^f(x, y) = \varepsilon_{ij}^c y_j + u_i^{(1)}(x, y) \tag{23.2}$$

where x is the macroscale position vector in the macroscale domain, y is the microscale position vector in the unit cell domain, ε_{ij}^{c} is the strain tensors in the macroscale domain, and $u_i^{(1)}(x,y)$ is the perturbation displacement of the microscale. The periodic boundary conditions [9] in the unit cell domain could be implemented by so-called "mixed boundary conditions" via constraint equations, is expressed by the following equations [9,17]:

$$\int_{\partial\Theta_Y}\left(u_i^f(x,y)-\varepsilon_{ik}^{c}y_k\right)N_j^{\Theta}d\gamma_Y=0 \tag{23.3}$$

$$\left|u_i^f(x,y)-\varepsilon_{ik}^{c}y_k\right|N_j^{\Theta}\leq Tol \tag{23.4}$$

where N_j^{Θ} is the unit normal to the unit cell boundary $\partial\Theta_y$.

23.3 Experiments

23.3.1 *Material tests*

The epoxy resin used in the tests is RenGel SW 404 with hardener HY 2404 at ambient temperature. Reinforcing steel particles are chosen as steel shot S330 with a nominal diameter of 0.84 mm. Compression tests on both unconfined and confined conditions were carried out. As is shown in Figs. 23.4 and 23.5, the dimensions of the unconfined specimen are 26 mm × 50 mm. The nominal dimensions of the confined specimen are 22 mm × 22 mm, confined by S235 steel tube with dimensions of 30mm × 50 mm × 4 mm and loaded by a S355 steel cylinder with dimensions of 22mm × 40 mm. Five specimens of each type, totaling 20 specimens, were prepared and tested in order to investigate the compressive behavior of resin and steel-reinforced resin. The load is applied with a displacement speed of 0.01 mm/s. Two GS-551 linear variable displacement transformers (LVDTs) were employed to measure the axial deformation of the specimens.

23.3.2 *Experimental results*

23.3.2.1 *Unconfined specimens*

The compressive results of unconfined resin and steel-reinforced resin specimens are summarized in Tables 23.1–23.4. It is noted that the true ultimate strength of unconfined resin is 17.6% smaller than the nominal ultimate strength. Attention should be paid to large differences between nominal and true ultimate compressive strength of resin during finite element simulation. The stress–strain relationship of unconfined resin and steel-reinforced resin specimens is shown in Figs. 23.6 and 23.7. The stress–strain curve of unconfined resin generally consists of three stages: (1) the stress increases linearly with strain increasing; (2) yielding occurs, the stress

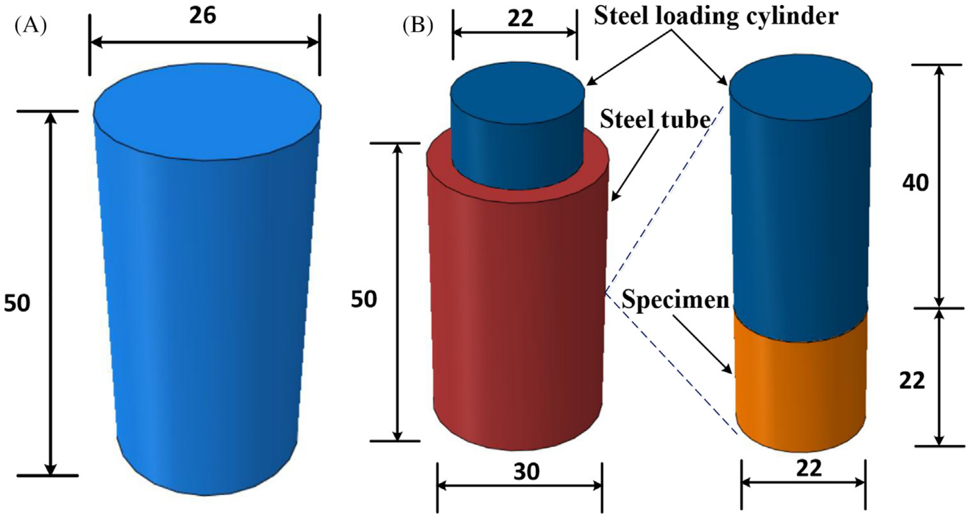

Figure 23.4 Schematic of unconfined/confined specimens: (A) unconfined; (B) confined.

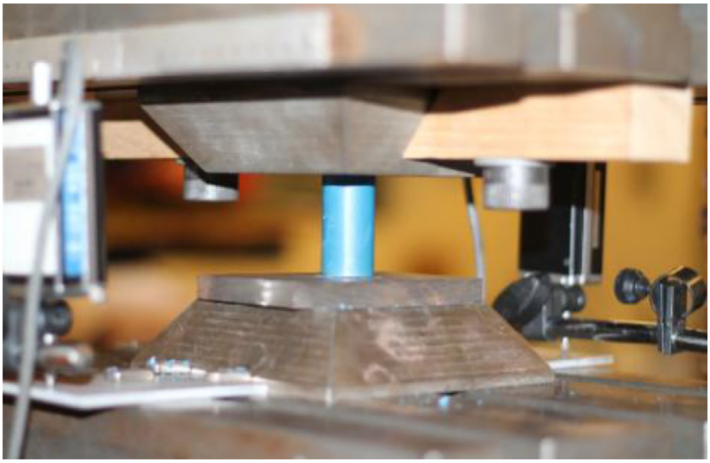

Figure 23.5 Experimental set-up.

Table 23.1 Results of unconfined resin specimen from nominal stress/strain.

Specimen	**Young's modulus**	**Ultimate strength**	**Fracture initiation strain**	**Fracture strain**
	$\bar{E}$ **(GPa)**	$\bar{\sigma}^u$ **(MPa)**	$\bar{\varepsilon}_0^f$ **(%)**	$\bar{\varepsilon}_u^f$ **(%)**
U-R-1	5.30	171.7	18.20	21.59
U-R-2	6.15	168.9	18.34	21.86
U-R-3	5.83	173.2	18.20	20.24
U-R-4	5.45	168.7	17.34	22.31
U-R-5	5.49	166.6	17.96	24.84
Average	5.64	169.8	18.01	22.17
S.D.	0.34	2.62	0.40	1.68

increases nonlinearly with increasing strain; and (3) fracture initiates when the resistance is reached, followed by a decrease in stress with an increase in strain. The stress–strain curve of unconfined steel-reinforced resin generally included two stages: (1) the stress increases almost linearly with increasing strain; and (2) damage occurs when the maximum strength is reached, followed by a decrease in stress with increasing strain.

The failure modes of resin and steel-reinforced resin specimens are shown in Fig. 23.8. The longitudinal and diagonal cracks of resin were initiated with increasing load. The final failure of resin occurred after the long cracks propagated through the whole specimen and the specimen was split into two. The diagonal cracks of steel-reinforced specimens were initiated from the bottom of the specimens. The steel-reinforced specimen failed when the diagonal cracks propagated to the bottom of the specimen.

Table 23.2 Results of unconfined resin specimen from true stress/strain.

Specimen	Young's modulus	Ultimate strength	Fracture initiation strain	Fracture strain
	E (GPa)	σ^u (MPa)	ε_0^f (%)	ε_u^f (%)
U-R-1	5.20	141.69	19.70	24.66
U-R-2	6.02	139.23	19.43	24.72
U-R-3	5.72	142.43	19.78	24.34
U-R-4	5.33	141.47	18.64	24.51
U-R-5	5.38	138.72	19.71	26.58
Average	5.53	140.71	19.45	24.96
S.D.	0.33	1.63	0.47	0.92

Table 23.3 Results of unconfined steel-reinforced resin specimen from nominal stress/strain.

Specimen	Young's modulus	Ultimate strength	Fracture initiation strain	Fracture strain
	$\overline{E}$ (GPa)	$\overline{\sigma}^u$ (MPa)	$\overline{\varepsilon}_0^f$ (%)	$\overline{\varepsilon}_u^f$ (%)
U-SR-1	15.90	117.97	0.97	3.86
U-SR-2	16.30	119.52	1.01	4.87
U-SR-3	15.50	124.13	0.94	3.97
U-SR-4	15.60	119.48	1.08	4.84
U-SR-5	15.10	122.14	1.03	4.98
Average	15.70	120.30	1.01	4.51
S.D.	0.41	2.72	0.054	0.54

Table 23.4 Results of unconfined steel-reinforced resin specimen from true stress/strain.

Specimen	Young's modulus	Ultimate strength	Fracture initiation strain	Fracture strain
	E (GPa)	σ^u (MPa)	ε_0^f (%)	ε_u^f (%)
U-SR-1	15.63	116.74	0.98	3.90
U-SR-2	15.72	118.32	1.02	4.98
U-SR-3	15.03	122.88	1.01	4.12
U-SR-4	15.16	118.27	1.09	4.92
U-SR-5	14.91	120.92	1.02	5.18
Average	15.29	119.43	1.03	4.62
S.D.	0.36	2.45	0.04	0.57

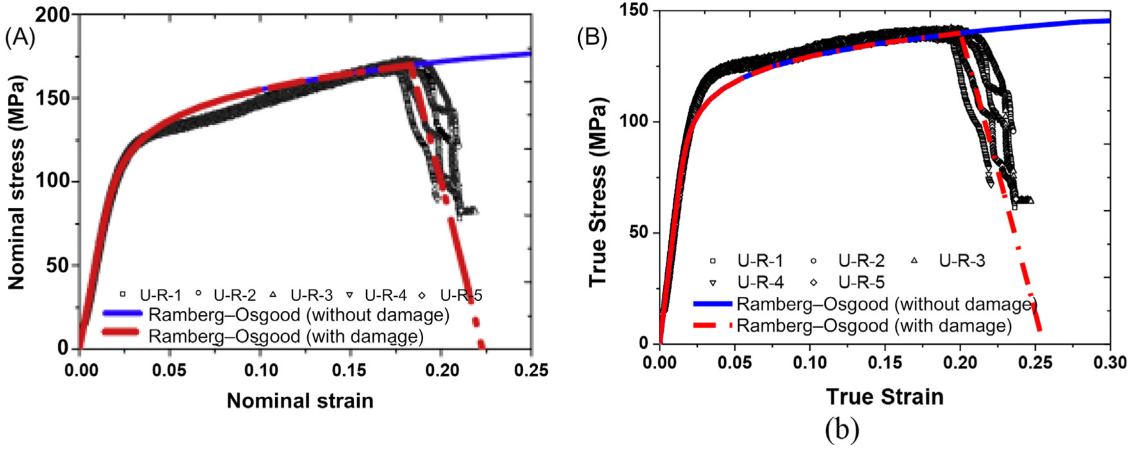

Figure 23.6 Stress–strain relationship of unconfined resin specimens: (a) Nominal stress versus nominal strain and (b) True stress versus true strain.

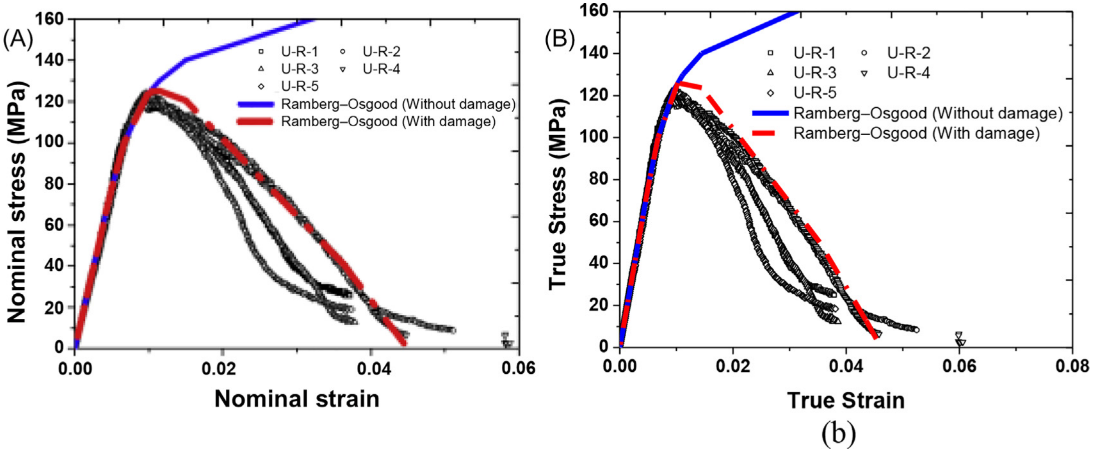

Figure 23.7 Stress–strain relationship of unconfined steel-reinforced resin specimens: (a) Nominal stress versus nominal strain and (b) True stress versus true strain.

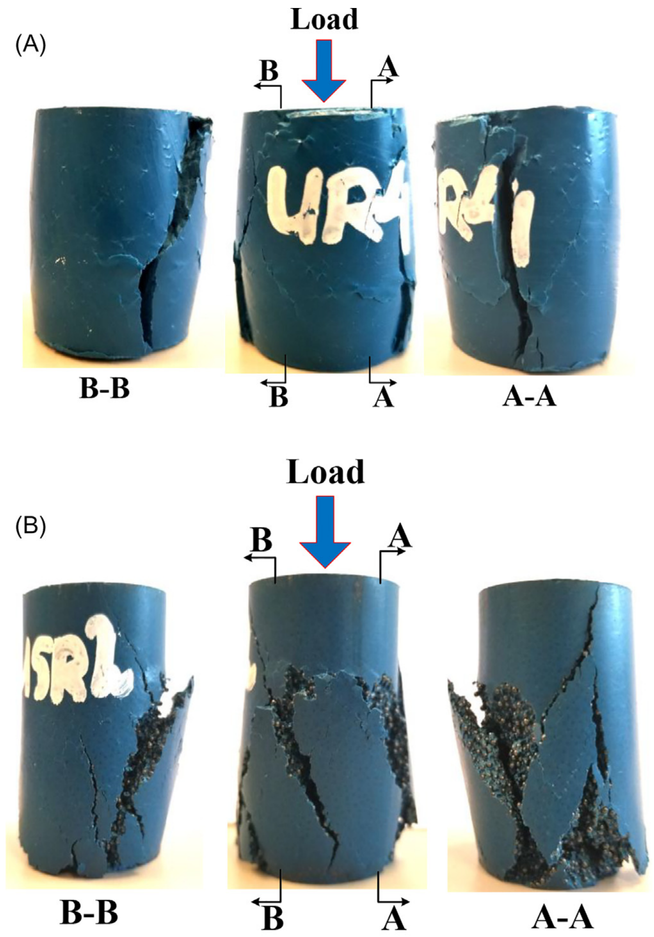

Figure 23.8 Typical failure mode for resin (A) and steel-reinforced resin (B).

23.3.2.2 *Confined specimens*

The compressive elastic moduli of confined resin and steel-reinforced resin specimens are summarized in Table 23.5. It is noted that the confined specimen is not loaded to ultimate failure and therefore the ultimate strength of the confined specimen is not obtained. The stress–strain relationships of confined resin and steel-reinforced resin are shown in Figs. 23.9 and 23.10. The stress–strain curve of confined specimens consists of two stages: (1) the stress increases linearly with strain increasing; and (2) yielding occurs, and the stress increases nonlinearly with increasing strain. The nonlinear branch of the stress–strain curve of confined specimen is due to: (1) the nonlinear behavior of the material itself, the yield surface of resin and steel-reinforced resin is hydrostatic pressure dependent; and (2) yielding

Table 23.5 Elastic modulus of confined resin and steel-reinforced resin.

Specimen	**Confined resin**		**Confined steel-reinforced resin**	
	$\overline{E}$ **(GPa)**	E **(GPa)**	$\overline{E}$ **(GPa)**	E **(GPa)**
C-1	6.84	6.66	17.99	17.61
C-2	6.84	6.52	19.56	19.36
C-3	7.15	6.91	19.59	19.43
C-4	7.66	7.59	18.66	18.45
C-5	8.09	7.78	16.18	15.96
Average	7.32	7.09	18.40	18.16
S.D.	0.54	0.56	1.41	1.44

of the confining steel tube, this leads to the situation where the resin is subject to a loss of confinement.

The deformation of the confined specimen is shown in Fig. 23.11. Obvious yielding is observed at the bottom half of the confined steel tube. The yielding of the steel tube is more pronounced in the case of the confined resin specimen compared to the confined steel-reinforced resin specimen, indicating that the Poisson's ratio of resin is larger than that of the steel-reinforced resin.

23.3.2.3 Results and discussion

The apparent Young's modulus increased by 29.7% for the confined resin specimens and increased by 7.5% for the confined steel-reinforced resin specimens. An explanation for the different increases in elastic modulus is that the Poisson's ratio of resin is larger than that of the steel-reinforced resin. The strength of confined specimens has obviously increased. The yield strength increased by 95.6% for confined resin specimens, and the yield strength increased by 189% for confined steel-reinforced resin.

It is assumed that the uniaxial compressive behavior is described by combining the damage mechanics and Ramberg–Osgood relationship [19], represented by:

$$\sigma = (1 - D)\sigma^{R-O}(\varepsilon) \tag{23.5}$$

$$\varepsilon = \frac{\sigma^{R-O}}{E} + K\left(\frac{\sigma^{R-O}}{E}\right)^{n} \tag{23.6}$$

where D is the damage variable.

The parameters of the Ramberg–Osgood relationship are fitted based on the experimental results before any damage occurred. The fitted material parameters are listed in Table 23.6. The comparisons of stress–strain relationship from the Ramberg–Osgood relationship and experimental results are shown in Figs. 23.6,

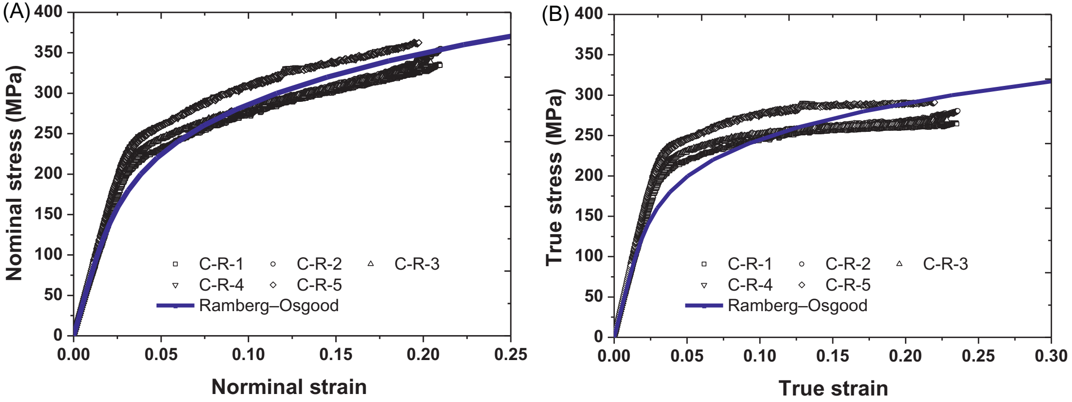

Figure 23.9 Stress−strain relationship of confined resin specimens: (a) Nominal stress versus nominal strain and (b) True stress versus true strain.

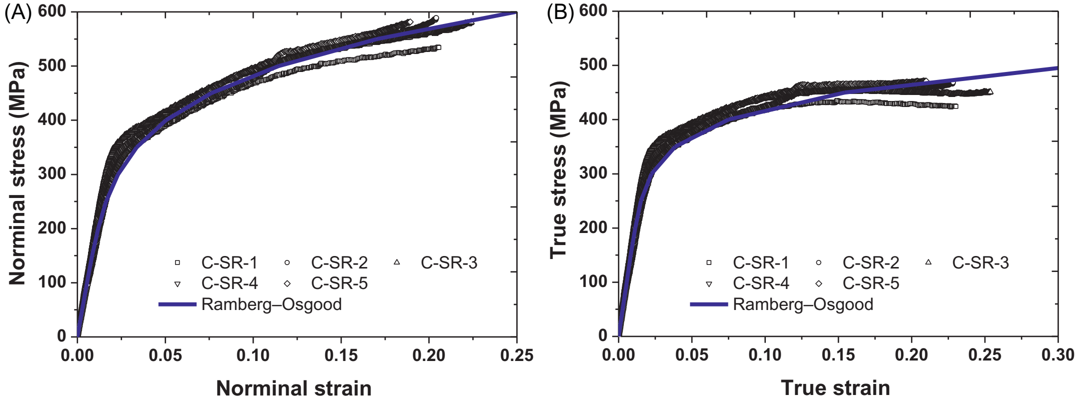

Figure 23.10 Stress−strain relationship of confined resin specimens: (a) Nominal stress versus nominal strain and (b) True stress versus true strain.

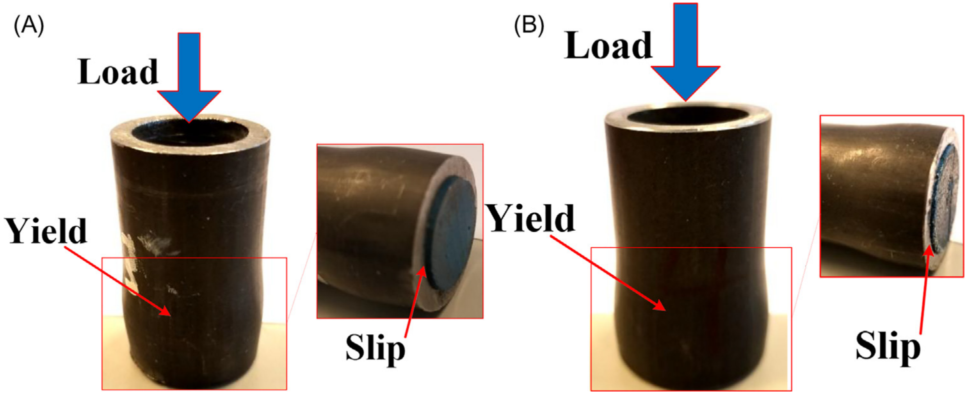

Figure 23.11 Deformation of confined specimens: (A) resin; (B) steel-reinforced resin.

Table 23.6 Ramberg–Osgood relationship parameters of resin and steel-reinforced resin.

Item		**K**	***n***	***R*²**
Unconfined resin	Nominal stress	6.07×10^{11}	8.27	0.98
	True stress	1.62×10^{16}	10.62	0.95
Unconfined steel-reinforced resin	Nominal stress	7.81×10^{15}	8.83	0.99
	True stress	4.43×10^{16}	9.15	0.94
Confined resin	Nominal stress	1.82×10^{5}	4.55	0.90
	True stress	3.28×10^{6}	5.27	0.85
Confined steel-reinforced resin	Nominal stress	5.68×10^{6}	4.99	0.97
	True stress	2.00×10^{11}	7.59	0.89

23.7, 23.9, and23.10. A good agreement is observed when no damage occurred. It is assumed that the fracture initiation occurred when the load reached the peak value. The damage variable is defined as:

$$D = \begin{cases} 0 & \varepsilon < \varepsilon_0^f \\ \dfrac{\varepsilon - \varepsilon_0^f}{\varepsilon_u^f - \varepsilon_0^f} & \varepsilon \geq \varepsilon_0^f \end{cases} \tag{23.7}$$

where ε_0^f is the plastic strain at fracture initiation, and ε_u^f is the plastic strain at the failure. The fracture initiation strain ε_0^f is assumed to be the corresponding strain at the peak load, while the failure strain is obtained by extended the softening stage. The values of ε_0^f and ε_u^f are listed in Tables 23.1–23.4, based on the experimental results. The comparisons between combined damage Ramberg–Osgood relationship and experimental results are shown in Figs. 23.6 and 23.7. A good agreement is observed.

23.4 Numerical simulation of resin

23.4.1 Unconfined resin simulation

The unconfined resin compressive tests were simulated numerically using the commercial finite element software ABAQUS/Standard [18]. The finite element model is shown in Fig. 23.12.

The linear Drucker–Prager model is employed to model the resin behavior. The friction angle β, the ratio of the yield stress in triaxial tension to the yield stress in triaxial compression K, and the dilation angle ψ are summarized in Table 23.7. The nominal stress–strain relationship of unconfined resin comparisons between finite element simulation and experimental results is shown in Fig. 23.13. A good agreement is observed, indicating that the material model could effectively model the uniaxial loading of unconfined resin.

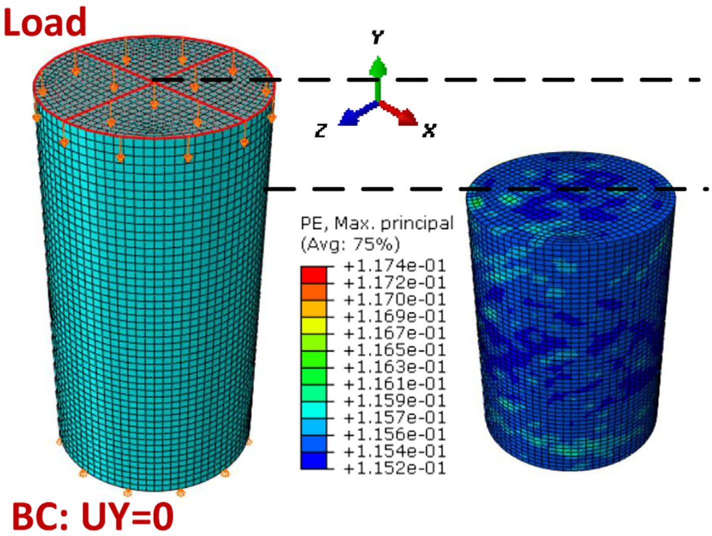

Figure 23.12 Finite element model of unconfined resin specimen.

Table 23.7 Material parameters of the linear Drucker–Prager model.

Material	**Associated flow**			**Nondilatant flow**		
	β	***K***	ψ	β	***K***	ψ
Resin	12.16°	0.92	12.16°	12.18°	1.00	0°
Steel-reinforced resin	49.80°	0.78	49.80°	52.04°	1.00	0°

23.4.2 Confined resin simulation

As shown in Fig. 23.14, a finite element model on confined resin tests was built to validate the efficiency of the linear Drucker–Prager model when predicting resin behavior with confinement. The nominal stress–strain relationship of confined resin comparisons between finite element simulation and experimental results is shown in Fig. 23.15. A good agreement is observed, indicating that the Drucker–Prager model could effectively model the confinement effects of resin. The deformation comparisons between FEM and experiments of confined resin are shown in Fig. 23.16.

23.5 Numerical simulation of steel-reinforced resin

23.5.1 Unconfined steel-reinforced resin

Due to the limit of the manufacturing process of steel-reinforced resin, it is difficult to make dog-shaped tensile specimens to obtain tensile behavior experimentally.

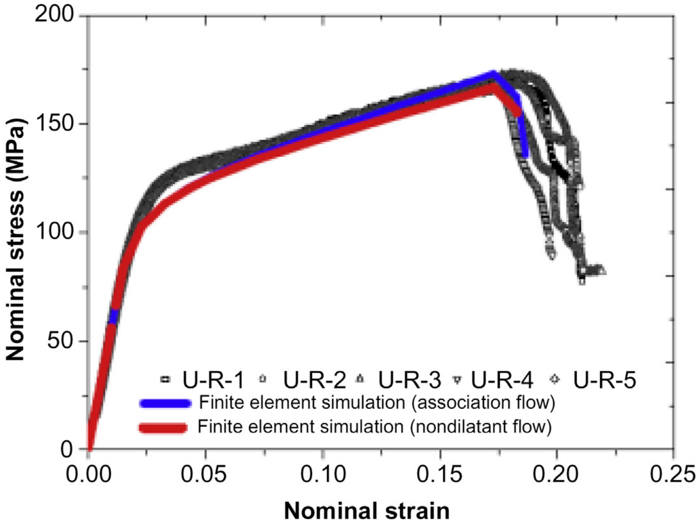

Figure 23.13 Stress–strain relationship comparisons between FEM and experiments of unconfined resin.

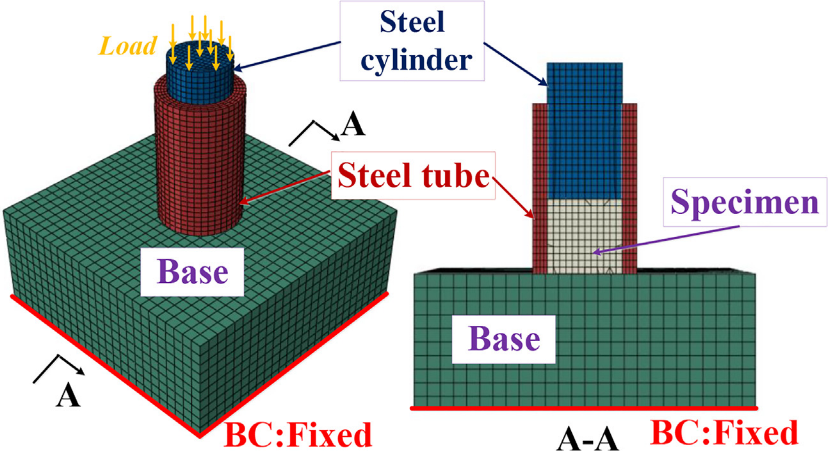

Figure 23.14 Finite element model of confined material tests.

The computational homogenization method provides an alternative way to obtain the tensile and shear behavior numerically after validating the multiscale model with compressive test results. The unit cell is shown in Fig. 23.17. The interface parameters are calibrated based on compressive test results. The normal interface stiffness is calibrated as 5.53×10^5 N/mm^3, and the shear interface stiffness is calibrated as 2.01×10^5 N/mm^3. The normal interface strength is calibrated as 40.8 MPa. The shear interface strength is calibrated to be 41.5 MPa. The normal

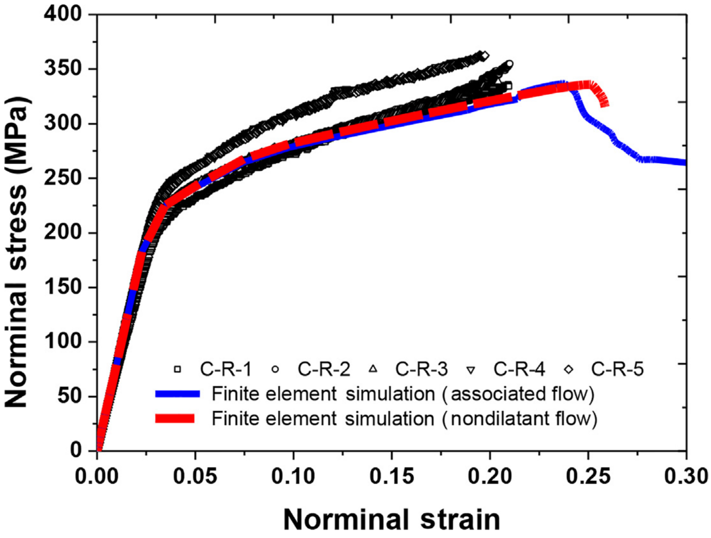

Figure 23.15 Stress−strain relationship comparisons between FEM and experiments of confined resin.

critical fracture energies G_n^c are determined as 0.04 kJ/mm, and the shear critical fracture energies G_s^c and G_t^c are determined as 0.45 kJ/mm. The material parameter is assumed to be 1.8. The viscosity coefficient for the cohesive surface is assumed to be 0.001 second.

Compressive stress−strain relationship comparisons between numerical homogenization and experiments of unconfined steel-reinforced resin are shown in Fig. 23.18. The macroscale stress is obtained based on Eq. (23.1), therefore the homogenization results are compared with the true stress−strain relationship. A good agreement is observed, indicating it is reliable to use the computational homogenization method to predict the tensile and shear behavior of steel-reinforced resin. The uniaxial stress−strain relationship and shear stress−strain relationship based on numerical homogenization method is shown in Fig. 23.19. The ultimate tensile strength of steel-reinforced resin is 39.8 MPa. The steel-reinforced resin material parameters of the linear Drucker−Prager model are summarized in Table 23.7.

The finite element simulation of unconfined steel-reinforced resin is shown in Fig. 23.20. The nominal stress−strain relationship of unconfined steel-reinforced resin and a comparison between finite element simulation and experimental results is shown in Fig. 23.21. A good agreement is observed.

23.5.2 Confined steel-reinforced resin

Similar to confined resin tests, a finite element model on confined steel-reinforced resin tests was built to validate the efficiency of the linear Drucker−Prager model

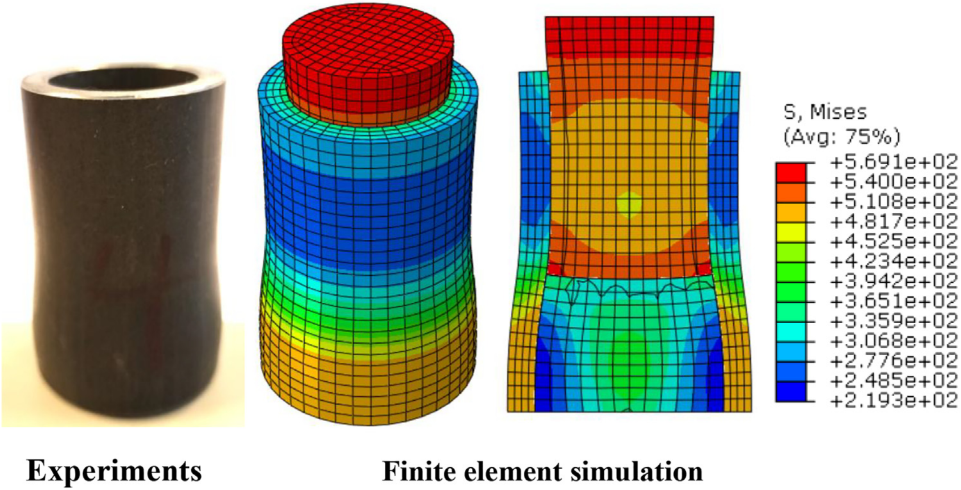

Experiments **Finite element simulation**

Figure 23.16 Deformation comparisons between FEM and experiments of confined resin.

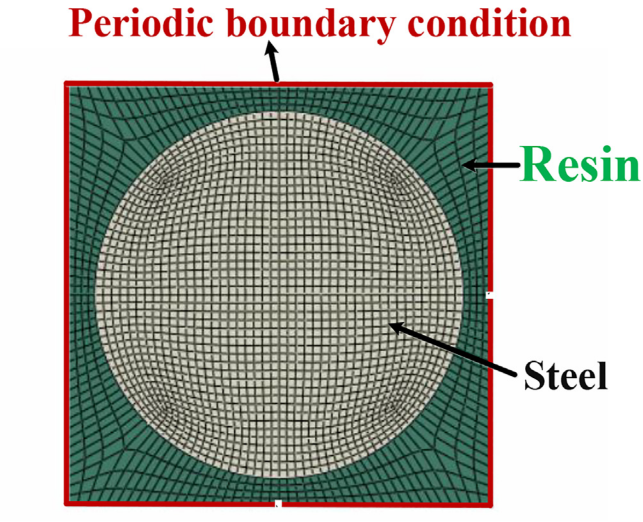

Figure 23.17 Unit cell of steel-reinforced resin.

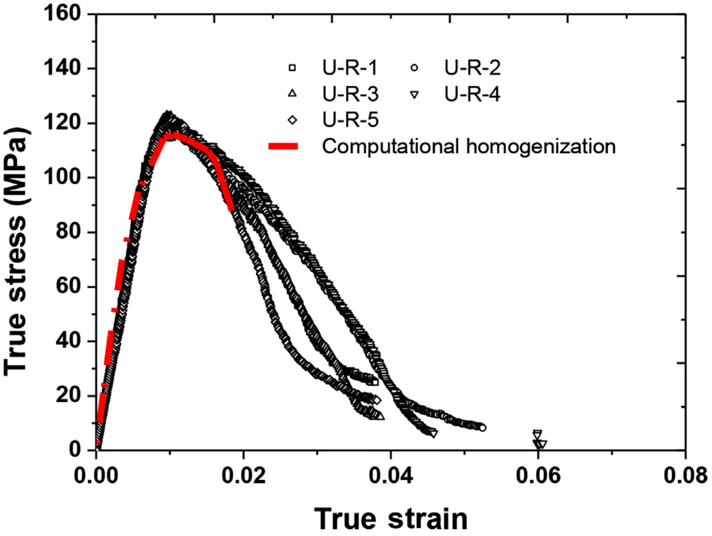

Figure 23.18 Stress−strain relationship comparisons between numerical homogenization and experiments of unconfined steel-reinforced resin.

when predicting steel-reinforced resin behavior with confinement. The nominal stress−strain relationship of confined steel-reinforced resin and a comparison between finite element simulation and experimental results is shown in Fig. 23.22. The finite element simulation results from an “associated flow” model agreed well

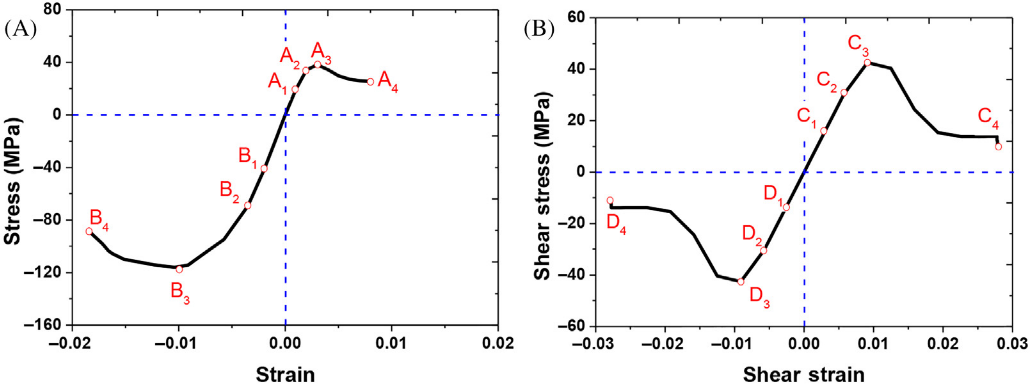

Figure 23.19 Stress−strain relationship of steel-reinforced resin from numerical homogenization: (A) Uniaxial stress versus uniaxial strain; (B) Shear stress versus shear strain.

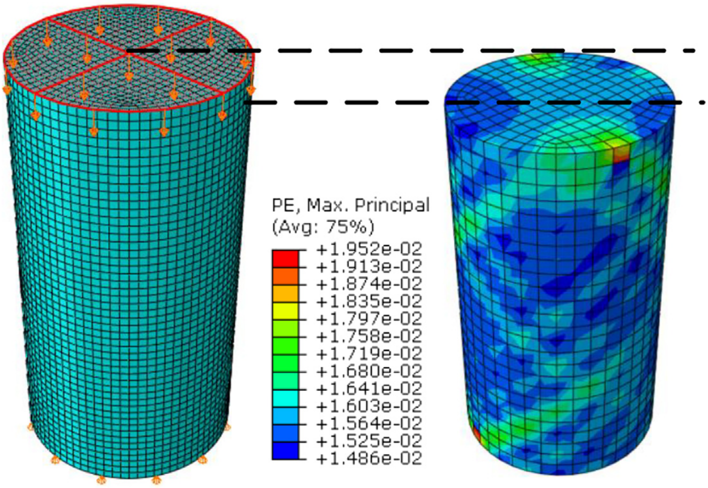

Figure 23.20 Finite element model of unconfined steel-reinforced resin specimen.

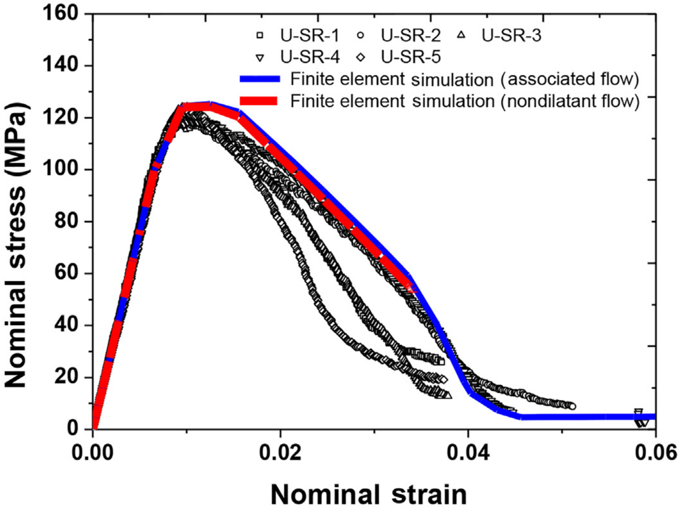

Figure 23.21 Stress−strain relationship comparisons between FEM and experiments of unconfined steel-reinforced resin.

with the experimental results, but the finite element simulation results from “nondilatant flow” tend to be smaller than the experimental results in the hardening stages. The Drucker−Prager models with “associated flow” rules predict the confinement effects of steel-reinforced resin efficiently. Fig. 23.23 showed deformation

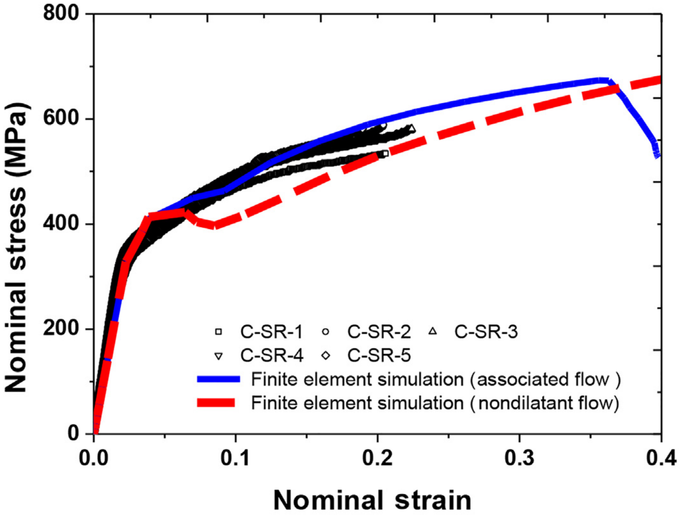

Figure 23.22 Stress—strain relationship comparisons between FEM and experiments of confined steel-reinforced resin.

comparisons of confined steel-reinforced resin tests between FEM and experiments. A good agreement is observed.

23.6 Conclusions

Compressive material tests on unconfined/confined resin and steel-reinforced resin were experimentally evaluated in order to validate the numerical results. Finite element simulation and multiscale homogenization methods were successfully used in this study to effectively model the material properties of resin and steel-reinforced resin.

1. A combined damage mechanics and Ramberg—Osgood relationship is proposed in this chapter to describe the uniaxial compressive behavior of resin and steel-reinforced resin. Related material parameters were fitted based on experimental results. The proposed uniaxial compressive model could effectively describe the uniaxial hardening/softening behavior of resin and steel-reinforced resin during finite element simulation.
2. The friction angle, the ratio of the yield stress in triaxial tension to the yield stress in triaxial compression K, and the dilation angle ψ of the linear Drucker—Prager plastic model are obtained based on experiments and numerical homogenization to efficiently consider the confinement effects on resin and steel-reinforced resin. The confinement effects on resin and steel-reinforced resin could be effectively simulated by combining the above parameters and a uniaxial compressive model. Finite element simulations on unconfined/confined resin and steel-reinforced resin material tests were conducted to validate the linear Drucker—Prager plastic model and material parameters proposed in this chapter. A good agreement is observed, indicating the model and parameters proposed in this chapter could be effectively used in the numerical simulation of injected bolted connections.

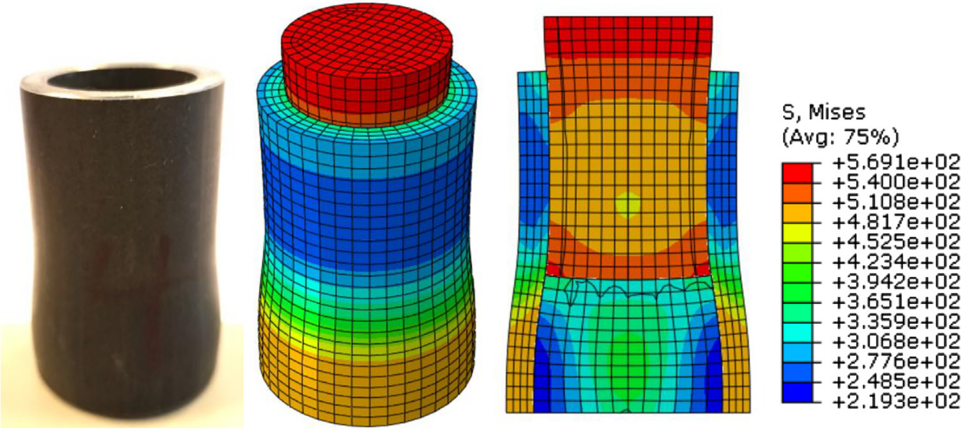

Experiments **Finite element simulation**

Figure 23.23 Deformation comparisons between FEM and experiments of confined steel-reinforced resin.

References

[1] B.D. Reid, Fastener Sealant Injection System, Google Patents, 1975.

[2] A.M.N. Gresnigt, J.W.B.J. Stark, Design of bolted connections with injection bolts, Connections in Steel Structures III, Elsevier, 1996, pp. 77−87.

[3] A.M. Gresnigt, G. Sedlacek, M. Paschen, Injection bolts to repair old bridges, Proceedings of Connections in Steel Structures IV, Citeseer, Roanoke, VA, 2000.

[4] C.M. Steenhuis, J.W.B. Stark, A.M. Gresnigt, Cost-effective connections, Prog. Struct. Eng. Mater. 1 (1) (1997) 18−24.

[5] A. Koper, Assessment of Epoxy Resins for Injected Bolted Shear Connections, Delft University and Technology, 2017.

[6] M.P. Nijgh, New Materials for Injected Bolted Connections, Delft University of Technology, 2017.

[7] ECCS, European Recommendations for Bolted Connections with Injection Bolts, ECCS Publication NO.79, Brussels, 1994.

[8] H. Kolstein, et al., Behaviour of double shear connections with injection bolts, Steel Constr 10 (4) (2017) 287−294.

[9] J. Fish, Practical Multiscaling, Wiley, 2013.

[10] H. Xin, A. Mosallam, Y. Liu, C. Wang, et al., Analytical and experimental evaluation of flexural behavior of FRP pultruded composite profiles for bridge deck structural design, Constr. Build. Mater., 150, 2017, pp. 123−149.

[11] H. Xin, Y. Liu, et al., Evaluation on material behaviors of pultruded glass fiber reinforced polymer (GFRP) laminates, Compos. Struct., 182, 2017, pp. 283−300.

[12] H. Xin, A. Mosallam, Y. Liu, Y. Xiao, et al., Experimental and numerical investigation on in-plane compression and shear performance of a pultruded GFRP composite bridge deck, Compos. Struct. 180 (2017) 914−932.

[13] H. Xin, A. Mosallam, Y. Liu, M. Veljkovic, J. He, Mechanical characterization of a unidirectional pultruded composite lamina using micromechanics and numerical homogenization, Construction and Building Materials 216 (2019) 101−118.

[14] H. Xin, M. Nijgh., M. Veljkovic, M, Computational homogenization simulation on steel reinforced resin used in the injected bolted connections, Composite Structures 210 (2019) 942−957.

[15] H. Xin, S. Sun, J. Fish, A surrogate modeling approach for additive-manufactured materials, Int. J. Multiscale Comput. Eng. 15 (6) (2017).

[16] H. Xin, W. Sun, J. Fish, Discrete element simulations of powder-bed sintering-based additive manufacturing, Int. J. Mech. Sci. 149 (2018) 373−392.

[17] J. Fish, R. Fan, Mathematical homogenization of nonperiodic heterogeneous media subjected to large deformation transient loading, June 2008, pp. 1044−1064. doi: 10.1002/nme.

[18] V. Abaqus, 6.14 Documentation, Dassault Systemes Simulia Corporation, 2014.

[19] W. Ramberg, W.R. Osgood, Description of stress-strain curves by three parameters, 1943, Report Number: NACA-TN-902. https://ntrs.nasa.gov/search.jsp?R = 19930081614.